Check for updates

Computational insights into Ir(III)-catalyzed allylic C−H amination of terminal alkenes: mechanism, regioselectivity, and catalytic activity†

Deng Pan,[a] Gen Luo, ID *[b] Yang Yu,[a] Jimin Yang[a] and Yi Luo ID *[ac]

Computational studies on Ir(III)-catalyzed intermolecular branch-selective allylic C−H amination of terminal olefins with methyl dioxazolone have been carried out to investigate the mechanism, including the origins of regioselectivity and catalytic activity difference. The result suggests that the reaction proceeds through generation of active species, alkene coordination, allylic C−H activation, decarboxylation, migratory insertion, and protodemetalation. The presence of $AgNTf_2$ could thermodynamically promote the formation of catalytically active species $[Cp*Ir(OAc)]^+$. Both the weaker Ir−C(internal) bond and the closer interatomic distance of N···C(internal) in the key allyl-Ir(V)-nitrenoid intermediate make the migratory insertion into Ir−C(internal) bond easier than into the Ir−C(terminal) bond, leading to branch-selective allylic C−H amidation. The high energy barrier for allylic C−H activation in the Co system could account for the observed sluggishness, which is mainly ascribed to the weaker coordination capacity of alkenes to the triplet $Cp*Co(OAc)^+$ and the deficient metal···H interaction to assist hydrogen transfer.
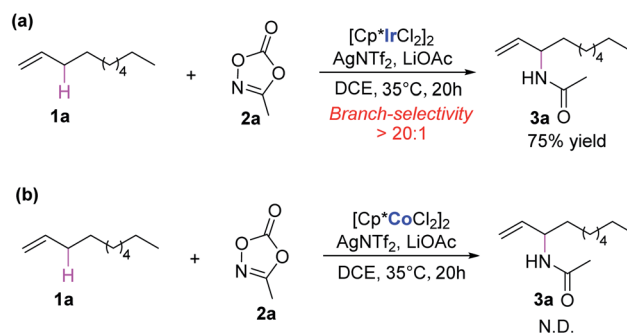
Introduction

Nitrogen-containing molecules are ubiquitous in natural products, synthetic intermediates, pharmaceuticals, and functional materials. Therefore, the construction of C–N bonds has been of fundamental importance for synthetic chemists in past decades.[1] In this context, transition-metal-mediated C–H aminations have become vital methods,[2,3] among which direct amination of the C–H bond is one of the most efficient ways, which could dramatically simplify synthetic routes, providing a straightforward and atom-economy methodology. Since the first report of transition-metal-catalyzed direct C–H amination,[4] remarkable advances have been made in this area both experimentally and theoretically.[5,6] Compared with chelate-assisted C–H amination, the allylic C–H amination is of great interest because the vinyl group is not only prevalent in large amounts of compounds but is also feasible for functionalization. Despite significant advances in this field, the precise control of the regioselectivity in the C–H amination reactions is still challenging.[7–10]

Recently, Rovis and co-workers reported an elegant work of Ir(III)-catalyzed intermolecular allylic C–H amination of unactivated terminal olefins using alkyl oxazolones as aminating agents, featuring excellent regioselectivity (Scheme 1a).[11] A

putative catalytic cycle was also proposed on the basis of relevant control experiments (Scheme 2). The monoacetato Cp*Ir(III) (OAc)$^+$(NTf$_2$)$^-$ (**I**), generated from [Cp*IrCl$_2$]$_2$, AgNTf$_2$, and LiOAc, was proposed as the catalytically active species. Alkene coordination gave the π-complex **II**, and metalation (C–H activation) formed allyl-Ir(III) species **III**. The subsequent oxidation of Ir(III) *via* N–O bond cleavage of oxazolone and CO$_2$ extrusion (decarboxylation) produced the allyl-Ir(V)-nitrenoid species **IV**. Subsequently, the regioselective migratory insertion and protodemetalation gave the branched amidation product and regenerate the active species **I**.

Despite the above mechanistic suggestions, many details are still ambiguous. Such as the reasonability of the proposed mechanism, the structural information on the key

[a] State Key Laboratory of Fine Chemicals, School of Chemical Engineering, Dalian University of Technology, Dalian 116024, China. E-mail: luoyi@dlut.edu.cn

[b] Institutes of Physical Science and Information Technology, Anhui University, Hefei 230601, China. E-mail: luogen@ahu.edu.cn

[c] PetroChina Petrochemical Research Institute, Beijing, 102206, China

Scheme 1 (a) Cp*Ir(III)- and (b) Cp*Co(III)-catalyzed allylic C–H amination of terminal alkene.
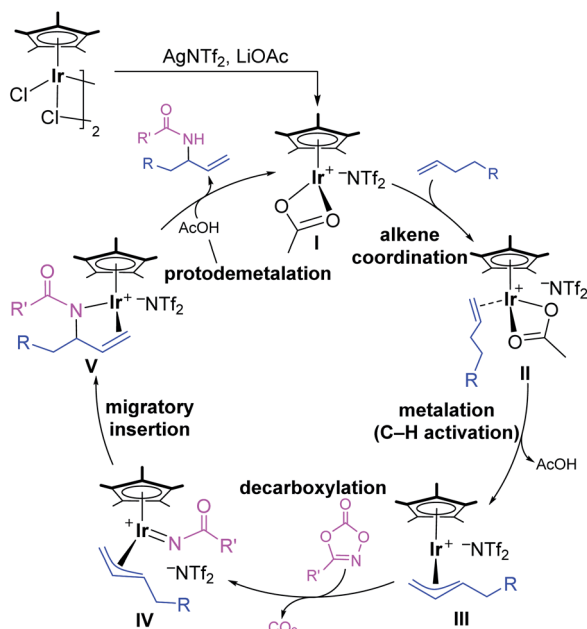
Scheme 2 Plausible mechanism for Ir(III)-catalyzed allylic C–H amination of terminal alkene.

intermediates and transition states, and the details of the energy profile. More importantly, the origin of regioselectivity for this important allylic C–H amination of unactivated terminal olefins remain unclear. In addition, it was also experimentally found that the reaction could not proceed when the analogue Cp*Co(III) was used as precatalyst (Scheme 1b). The origin of such distinct catalytic activity of these two similar precatalysts was also unknown. To clarify these issues, we performed density functional theory (DFT) calculations on the model reaction of Ir(III)/Co(III)-catalyzed intermolecular allylic C–H amination reaction of 1-decene (**1a**) with methyl dioxazolone (**2a**) (Scheme 1). The related mechanism has been carefully explored and some interesting results were obtained on the origins of regioselectivity and catalytic activity. The results reported here are expected to enrich the Ir(III)-catalyzed C–H amination of olefins and provides useful information for the development of new transition-metal-catalyzed regioselective C–H amination systems.

Computational details

All calculations were conducted using the Gaussian 16 program package.[12] The hybrid B3LYP functional[13] corrected with the empirical dispersion term (known as Grimme-D3 with the zero-damping scheme)[14] was used for geometry optimizations of all stationary points. In the optimizations, the 6-31G(d,p) basis set was used for C, H, N, and O atoms, and the SDD pseudopotential basis sets[15] were considered for metal atoms. Geometrical parameters for the stationary points were fully optimized without any constraints. Vibrational frequency analyses were performed on the optimized geometries at the same level of theory to characterize the stationary points as local minima (no imaginary frequency) or transition states (only one imaginary

frequency). Intrinsic reaction coordinate (IRC) calculations were used to verify that the transition state connects with appropriate reactant and product. To obtain more accurate energies, single-point calculations were further performed at the higher level of B3LYP-D3/def2-TZVP[16] together with the SMD solvation model[17] for considering the dichloroethane solvation effect. The free energies in solution reported in this study include the free-energy corrections calculated by the vibrational frequency analyses. In addition, the minimum-energy crossing point (MECP) was optimized using the code developed by Harvey and co-workers.[18] Three-dimensional structures were showed using the CYLview software.[19]

Results and discussion

Formation of active species

It was experimentally found that the precatalyst [Cp*IrCl$_2$]$_2$ was ineffective without adding additional AgNTf$_2$. This drove us to investigate the role of AgNTf$_2$ and the formation of active species. Under the experimental conditions,[11] various Ir(III) species (*e.g.*, Cp*Ir(OAc)$_2$, Cp*Ir(OAc)(NTf$_2$), [Cp*Ir(OAc)]$^+$ + X$^-$ (X$^-$ = OAc$^-$ and NTf$_2^-$), and [Cp*Ir(NTf$_2$)]$^+$ + OAc$^-$) may exist in the presence of precatalyst [Cp*IrCl$_2$]$_2$, AgNTf$_2$, and LiOAc. As shown in Scheme 3, in the absence of AgNTf$_2$, the formation of neutral Cp*Ir(OAc)$_2$ is endergonic by 16.3 kcal mol^{-1} (eqn (1)). The dissociation of an anion OAc$^-$ from Cp*Ir(OAc)$_2$ to give cationic [Cp*Ir(OAc)]$^+$ together with OAc$^-$ is further endergonic ($\Delta G = 31.2$ kcal mol^{-1}, eqn (2)), suggesting that it is an energetically inaccessible process. It is worth noting that, when AgNTf$_2$ was introduced, the formation of neutral Cp*Ir(OAc) (NTf$_2$) is less endergonic ($\Delta G = 9.3$ kcal mol^{-1}, eqn (3)) and the dissociation of NTf$_2^-$ from Cp*Ir(OAc) (NTf$_2$) to give cationic [Cp*Ir(OAc)]$^+$ is only endergonic by 8.7 kcal mol^{-1} (eqn (4)). In
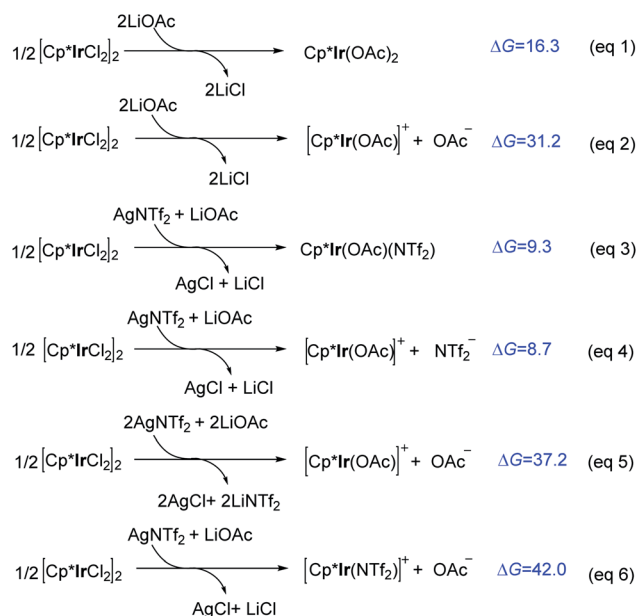
Scheme 3 Calculated reaction free energies (ΔG, kcal mol^{-1}) for the formation of various Ir(III) species.

addition, the formation of $[Cp*Ir(OAc)]^+$ or $[Cp*Ir(NTf_2)]^+$ *via* two molecules of LiOAc and AgNTf$_2$ was also calculated and was ruled out due to the relatively high reaction free energy ($\Delta G =$ 37.2 kcal mol^{-1}, eqn (5); $\Delta G =$ 42.0 kcal mol^{-1}, eqn (6)). Taken together with the above calculations, we can conclude that the cationic $[Cp*Ir(OAc)]^+$ species should be the active species involved in further catalytic cycle. And, AgNTf$_2$ play an important role in thermodynamically promoting the formation of $[Cp*Ir(OAc)]^+$. These computational results could provide a preliminary understanding on the role of AgNTf$_2$ additive and the formation of active species $[Cp*Ir(OAc)]^+$.

Matalation (allylic C–H activation) and decarboxylation

According to previous studies and above discussions, the cationic species $[Cp*Ir(OAc)]^+$ (**Ir-1**) with unsaturated coordination environment should be the active species, which promotes the alkene coordination and further activation. As shown in Fig. 1, the coordination of 1-decene (**1a**) to $[Cp*Ir(OAc)]^+$ (**Ir-1**) could form the more stable π-complex **Ir-2**. This step is exergonic by 4.3 kcal mol^{-1}. To achieve allylic C–H activation, **Ir-2** firstly isomerizes to **Ir-2′** *via* changing the coordination mode of acetate from κ2 to κ1 and forming an agostic interaction Ir⋯H–C instead.[20] Such an isomerization step *via* **Ir-TS$_{iso}$** has an energy barrier of 10.9 kcal mol^{-1} and is endothermic by 10.2 kcal mol^{-1}. Then, C–H activation in **Ir-2′** takes place through a traditional concerted metalation deprotonation (CMD) transition state **Ir-TS3** to give the η^3-allyl-Ir(III) intermediate **Ir-4**. The relative activation energy for C–H activation process is 19.6 kcal mol^{-1}, which should be kinetically reasonable under the experimental condition (35 °C).[11] Starting from **Ir-4**, the coordination of methyl-1,4,2-dioxazol-5-one (**2a**)

to the Ir(III) center of η^3-allyl-Ir(III) intermediate **Ir-4** is exergonic by 0.8 kcal mol^{-1}, giving the intermediate **Ir-5** for further C–N bond formation. Subsequently, the decarboxylation (CO$_2$ extrusion) easily takes place *via* **Ir-TS6** to yield the allyl-Ir(V)-nitrenoid **Ir-7**. The step has a low energy barrier of 4.0 kcal mol^{-1} and is highly exothermic by 21.5 kcal mol^{-1} (relative to the precatalyst and substrates). Such low energy barrier could be ascribed to the unique binding feature between the dioxazole moiety and the Ir center.[21] By comparison, the CO$_2$ extrusion from free methyl dioxazolone (**2a**) was calculated and encountered a high energy barrier (33.6 kcal mol^{-1}, Fig. S4†).

Migratory insertion (C–N formation) and protodemetalation

After the formation of allyl-Ir(V)-nitrenoid intermediate **Ir-7**, there are two potential sites for migratory insertion (Fig. 2), *viz.*, terminal (C1, leading to the linear amidation product) or internal position (C3, leading to the branched amidation product). As we can see from Fig. 2, the migratory insertion takes place at the C3 site (*via* **Ir-TS8**, black line) is more favorable than C1 site (*via* **Ir-TS8′**, blue line) by 3.5 kcal mol^{-1} and is an irreversible process, which is well in line with the regioselectivity observed experimentally.

Starting from the preferred migratory insertion product **Ir-9**, the coordination of a molecule of AcOH, which is formed in the C–H activation step (Fig. 1), could form the adduct **Ir-10** and then the protodemetalation of amination product takes place *via* a barrierless transition state **Ir-TS11** to give the final branched product **P-C3** and regenerates the active species **Ir-1**. As discussed above, the computational results generally support the proposed mechanism, which mainly involves the generation of the active species $[Cp*Ir(OAc)]^+$ with the aid of AgNTf$_2$, alkene coordination, allylic C–H activation (matalation) giving η^3-allyl-
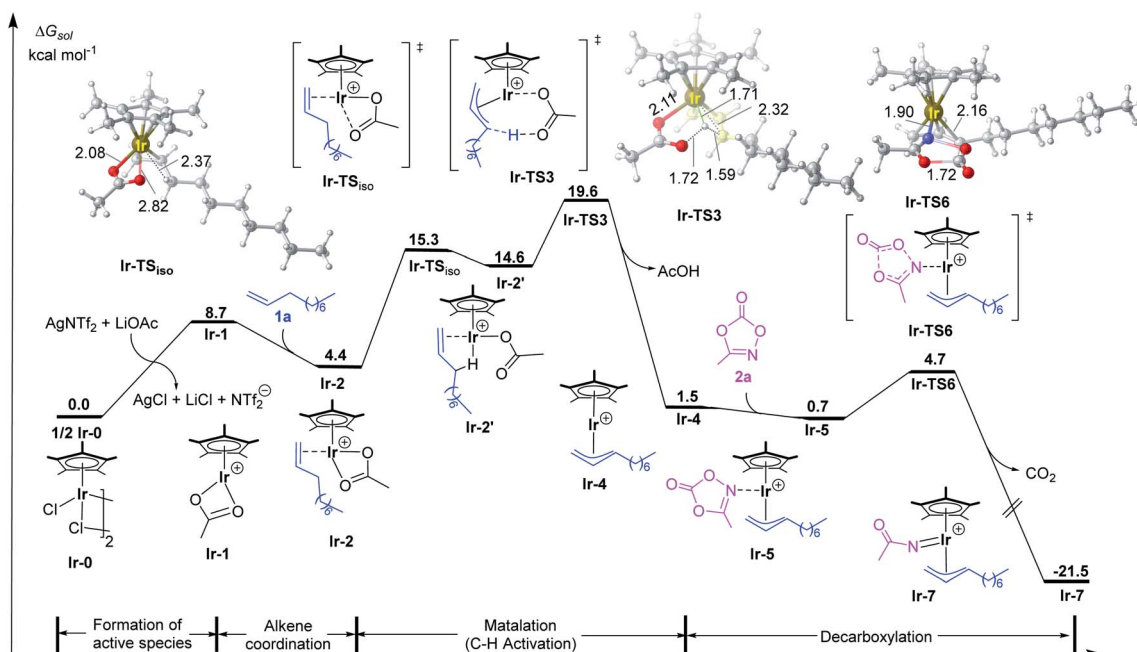

Fig. 1 Calculated free energy profiles for allylic C–H activation by the Ir(III) catalyst. Bond distances shown in the structures are given in angstroms.
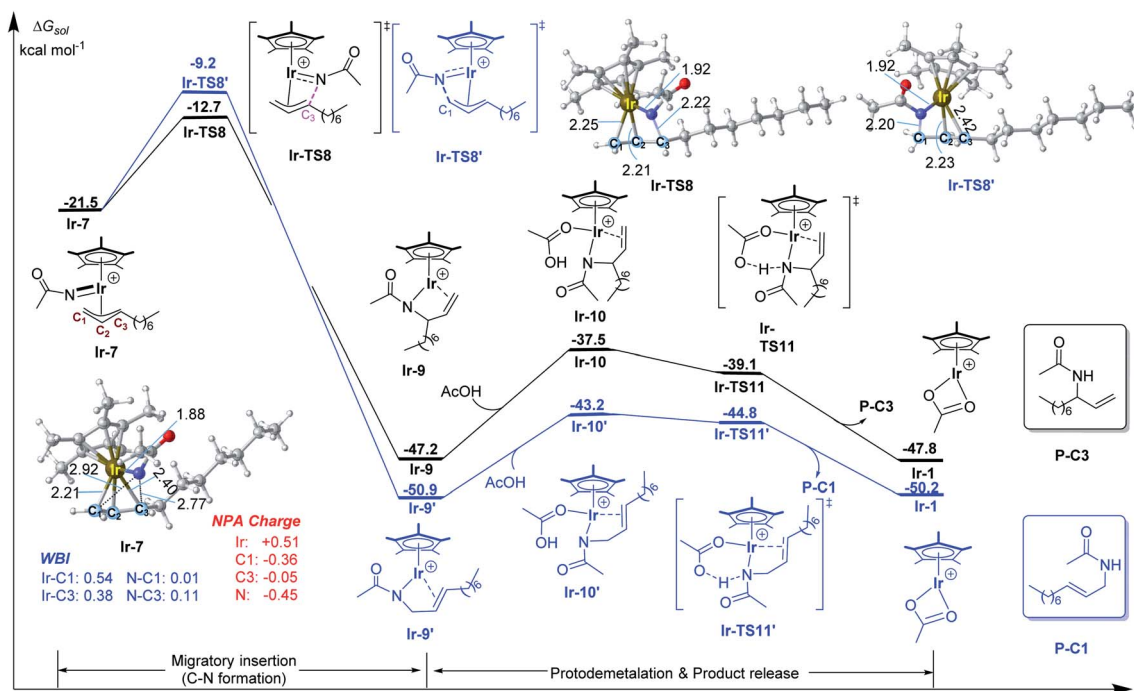
Fig. 2 Calculated free energy profiles for C–N bond formation by the Ir(III) catalyst. Bond distances shown in the structures are given in angstroms.

Ir(III) intermediate, decarboxylation forming the key Ir(V)-nitrenoid species, regioselective migratory insertion (C–N formation), and the final protodemetalation producing the amidation product and regeneration of the active species.

Origin of regioselectivity

To have a better understanding of the regioselectivity, the structure of **Ir-7** was carefully examined (Fig. 2). It is found that the Ir–C1 bond is stronger than Ir–C3 bond, reflected by the shorter bond distance of Ir–C1 (2.21 vs. 2.40 Å of Ir–C3) and the larger Wiberg bond indexes

(WBI) for Ir–C1 (0.54 vs. 0.38 for Ir–C1). This suggests that the migratory insertion into Ir–C3 bond is easier than Ir–C1 bond. In addition, the interatomic distance N···C3 (2.77 Å) is shorter than N···C1 (2.92 Å), which will also support more favorable N–C3 formation compared with N–C1. Therefore, both the weaker Ir–C3 bond and the shorter interatomic distance of N···C3 make the migratory insertion into Ir–C3(internal) bond easier than Ir–C1(terminal) bond, leading to branch-selective allylic C–H amidation.

For a comparison, the migratory insertion in the case of Rh catalyst was also calculated. As displayed in Fig. 3, although the
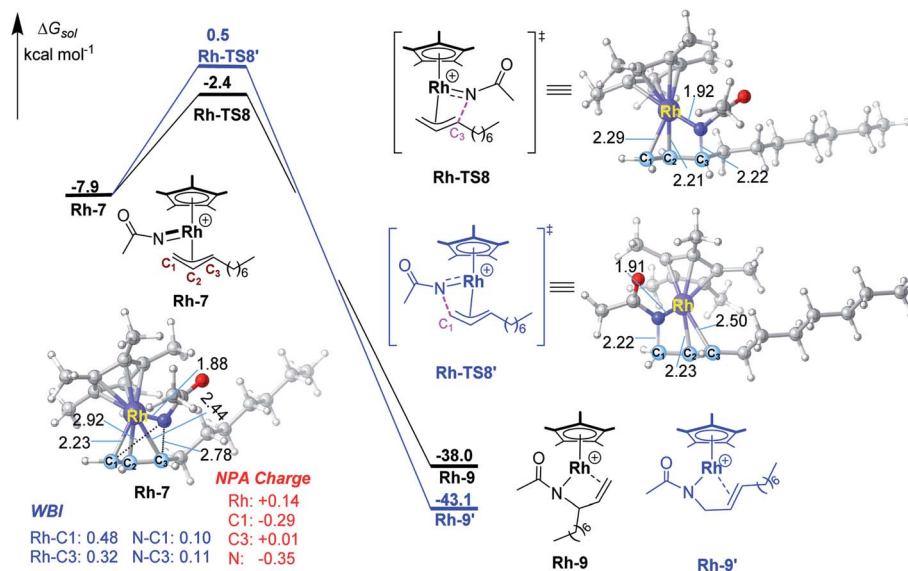

Fig. 3 Calculated free energy profiles for migratory insertion by the Rh(III) catalyst. Bond distances shown in the structures are given in angstroms.
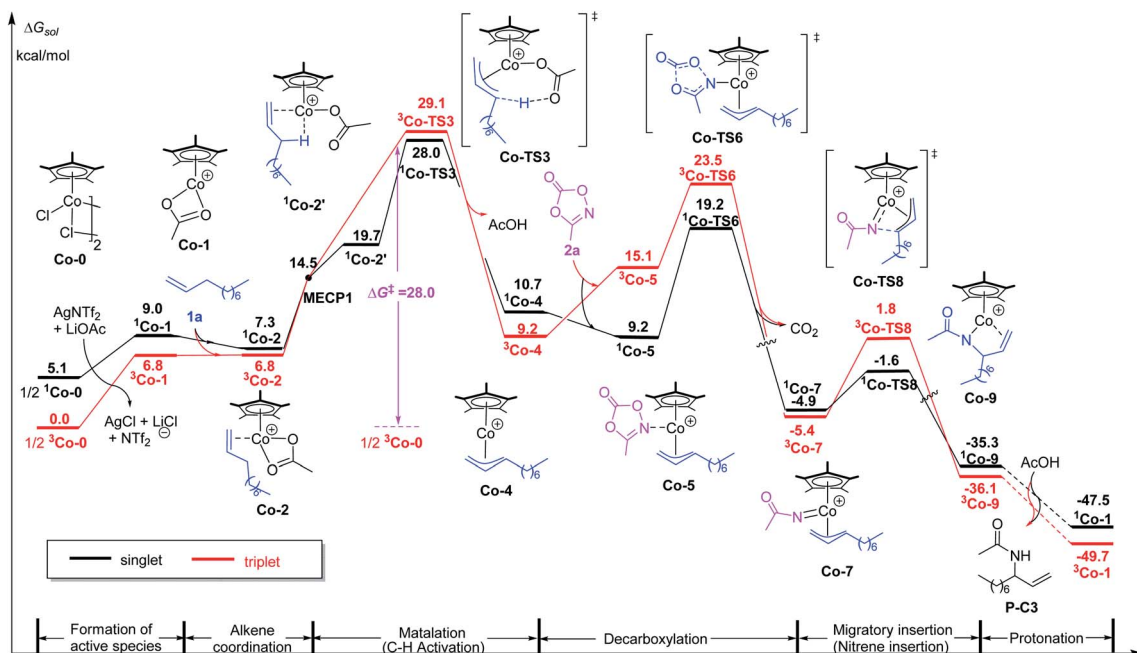
Fig. 4 Calculated free energy profiles for intermolecular allylic C–H amidation of 1-decene by the Co(III) catalyst.

migratory insertion takes place at the C3 site (*via* **Rh-TS8**) is more favorable than C1 site (*via* **Rh-TS8′**) by 2.9 kcal mol⁻¹, the energy difference is smaller than that in Ir case (3.5 kcal mol⁻¹), which is in general agreement with the observed lower regioselectivity in Rh system (2.9 : 1 for Rh *vs.* > 20 : 1 for Ir).[11] In **Rh-7**, similar to Ir case, the Rh–C1 (WBI: 0.48) bond is stronger than Rh–C3 (WBI: 0.32) bond, which could account for the superiority of migratory insertion into Rh–C3. To be noted, in contrast to **Ir-7**, the bond index of N–C3 (0.11) is similar to N–C1 (0.10) in **Rh-7**, which will lower the regioselectivity in comparison with Ir system. The smaller difference in NPA charge between N and C3 in **Rh-7** than that in **Ir-7** could be also account for the observed different regioselectivity.

Catalytic activity of different catalyst

Although [Cp*IrCl₂]₂ as a precatalyst works for such kind of C–H amination, the analogue [Cp*CoCl₂]₂ failed to produce any amidation products under the same experimental conditions. To elucidate the origin of such a reactivity difference, we carried out DFT calculations for the case of [Cp*CoCl₂]₂. Firstly, similar to the case of [Cp*IrCl₂]₂, the free energy of the formation of active species [Cp*Co(OAc)]⁺ was calculated. The result shows that the triplet is the ground state of [Cp*CoCl₂]₂ and is more stable than its singlet by 5.1 kcal mol⁻¹. In the case of triplet, the formation free energy of [Cp*Co(OAc)]⁺ is 6.8 kcal mol⁻¹ (Fig. 4), which is lower than that the case of Ir (8.7 kcal mol⁻¹). Therefore, the difference of catalytic activity between the two cases (Ir and Co systems) cannot be explained by the formation of active species.

Subsequently, the energy profile of Cp*Co(III)-catalyzed terminal alkene C–H amidation reaction was further calculated. The results show that Cp*Co(III)-catalyzed process is similar to

that of Cp*Ir(III). It is also worth noting that Co-catalyzed process follows a two-state reactivity scenario (Fig. 4). Unsurprisingly, the allylic C–H activation of terminal olefin have an energy barrier of 28.0 kcal mol⁻¹, which is significantly higher than that for Ir case ($\Delta G^{\ddagger}$ = 19.6 kcal mol⁻¹, Fig. 1). The high energy barrier of allylic C–H activation for Co catalyst could account for its catalytic sluggishness. Such a high energy barrier could be ascribed to the relatively unstable alkene-coordinating π-complex and the less stable transition state **¹Co-TS3** in comparison with Ir system.

As for the alkene-coordinating π-complex, the coordination of an alkene to **³Co-1** giving **³Co-2** is an isoenergetic process (Fig. 4), but it is an exothermic process for Ir system (*ca* 4.3 kcal mol⁻¹, Fig. 1) which could effectively lower the energy platform. To shed light on the different relative stability of the two π-complexes **Ir-2** and **³Co-2**, distortion/interaction
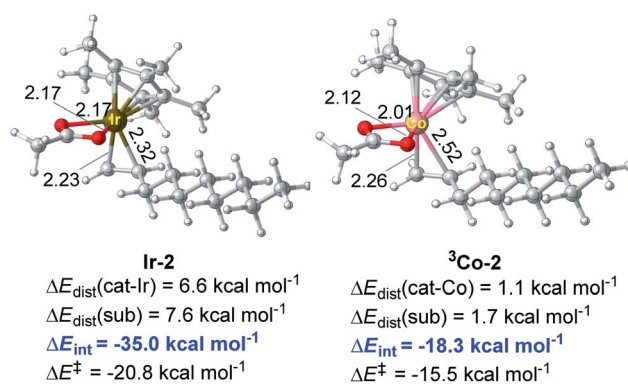

Fig. 5 Optimized structures of π-complexes **Ir-2** and **³Co-2** and their distortion/interaction analysis. Bond distances shown in the structures are given in angstroms (Å).
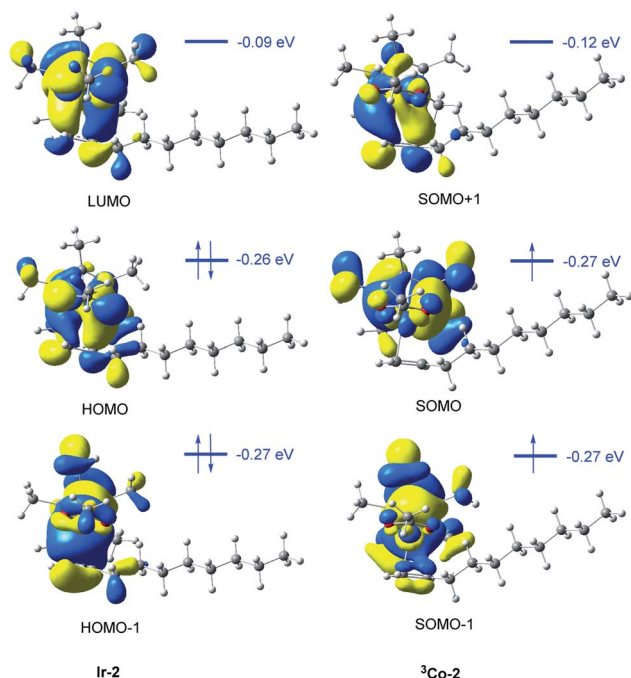
Fig. 6 Frontier molecular orbital analysis of alkene-coordinating π-complexes **Ir-2** and **³Co-2**.

Fig. 7 Optimized transition state structures of **Ir-TS3** and **¹Co-TS3**. The bond distances shown in the structures are given in angstroms (Å).

analysis[22] has been conducted (Fig. 5). In such analysis, each π-complex structure was divided into two fragments, *viz.*, the coordinating alkene part (fragment sub) and the remaining metal moiety (fragment cat-M). ΔE_{dist} is the energy required to distort separated fragments from their equilibrium geometry into the olefin-coordinated π-complexes. This energy is regarded as the destabilizing factor from geometry distortion. ΔE_{int} denotes the interaction energy between the fragments in the π-complex. The energy $\Delta E^{\ddagger}$ is defined as $\Delta E^{\ddagger} = \Delta E_{dist}(cat) + \Delta E_{dist}(sub) + \Delta E_{int}$. As shown in Fig. 5, although the distortion energies of the two fragments in **Ir-2** ($\Delta E_{dist}(cat\text{-}Ir) = 6.6$ kcal mol^{-1} and $\Delta E_{dist}(sub) = 7.6$ kcal mol^{-1}) are larger than that in **³Co-2** ($\Delta E_{dist}(cat\text{-}Co) = 1.1$ kcal mol^{-1} and $\Delta E_{dist}(sub) = 1.7$ kcal mol^{-1}), the interaction between the two fragments in **Ir-2** ($\Delta E_{int} = -35.0$ kcal mol^{-1}) is significantly stronger than that in **³Co-2** ($\Delta E_{int} = -18.3$ kcal mol^{-1}) by -16.7 kcal mol^{-1}, making **Ir-2** more stable than **³Co-2**. Therefore, it is the discriminatory strength of interaction that causes the different relative stability of the two π-complexes **Ir-2** and **³Co-2**.

The frontier molecular orbitals of the two π-complexes could also provide valuable information to explain their relative stability (Fig. 6). In the case of **Ir-2**, there is strong orbital interaction between the metal center and alkene part. For instance, the HOMO-1 orbital is the σ binding orbital which is composed of the d orbital of Ir and π-bonding orbital of the alkene. The HOMO orbital is the back donation π-binding orbital, which is composed of the d orbital of Ir and π*-bonding orbitals of alkene moiety. The electrons in HOMO and HOMO-1 orbitals are localized in the d orbital of the metal atom and alkene moiety in **Ir-2**. However, in **³Co-2**, only a ve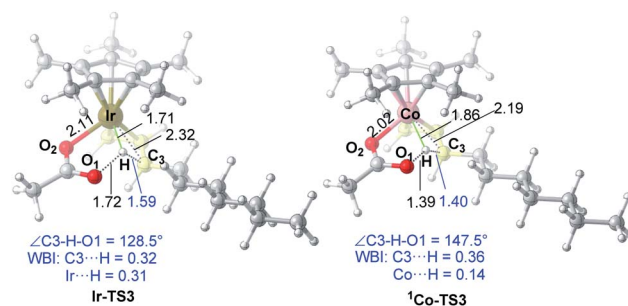ry small number of electrons in SOMO and SOMO-1 orbitals are localized in the Co-d orbital and alkene moiety. This may be due to the high spin of **³Co-2**, which makes the metal center has fewer empty d orbitals, so that the d orbital cannot accept more electrons. Meanwhile, the single electron in Co-d orbital has the Pauli repulsion to the alkene electrons. Therefore, the coordination capacity of alkene in **³Co-2** is weaker than that in **Ir-2**.

As for the C–H activation transition state, the singlet **¹Co-TS3** is slightly lower than **³Co-TS3** by 1.1 kcal mol^{-1} and the spin-crossing process occurs before C–H activation. The net energy barrier from π-complex **³Co-2** to **¹Co-TS3** is 21.2 kcal mol^{-1}, while the energy barrier in Ir system is 15.2 kcal mol^{-1} (**Ir-2 → Ir-TS3**, Fig. 1). To get more information on the difference of C–H activation process in two systems, the structures of **Ir-TS3** and **¹Co-TS3** are carefully compared (Fig. 7). As displayed in Fig. 7, it is found that the C3–H bond is more activated in **Ir-TS3** than that in **¹Co-TS3**, manifested by the longer bond distance ($d_{(C3\cdots H)} = 1.59$ Å in **Ir-TS3** *vs.* $d_{(C3\cdots H)} = 1.40$ Å in **¹Co-TS3**) and smaller bond index (WBI$_{(C3\cdots H)} = 0.32$ in **Ir-TS3** *vs.* WBI$_{(C3\cdots H)} = 0.36$ in **¹Co-TS3**). Importantly, the metal center plays a vital role in hydrogen transfer process. The results show that although the atomic radius of Ir is larger than Co, the distance of Ir···H in **Ir-TS3** (1.71 Å) is shorter than $d_{(Co\cdots H)}$ in **¹Co-TS3** (1.86 Å), suggesting that the stronger metal···H interaction exists in **Ir-TS3** compared to **¹Co-TS3**. The WBI values of metal···H (WBI$_{(Ir\cdots H)} = 0.31$ in **Ir-TS3** *vs.* WBI$_{(Co\cdots H)} = 0.14$ in **¹Co-TS3**) and the tortile angles of C3–H–O1 (128.5° in **Ir-TS3** *vs.* 147.5° in **¹Co-TS3**) could further illustrate the aforementioned reactivity difference in the two catalytic systems.

On the basis of above discussion, the high catalytic activity of Ir catalyst is mainly attributed to the relative stability of alkene-coordinating π-complex and the stronger metal···H interaction assisting hydrogen transfer in comparison with Co system. In addition, Ir-catalyzed C–H activation process is exothermic, while it is an endothermic process for Co system. Consequently, Cp*Ir(III)-catalyzed allylic C–H activation of terminal alkene is more favorable than Cp*Co(III) both thermodynamically and kinetically.

Conclusions

In summary, Cp*Ir(III)-catalyzed allylic C–H amination reaction of 1-decene with methyl dioxazolone has been investigated by DFT calculations. The computational results suggest that the

reaction mainly includes the following steps: the formation of active species $[Cp*Ir(OAc)]^+$, alkene coordination, allylic C–H activation (matalation) giving η^3-allyl-Ir(III) intermediate, decarboxylation of methyl dioxazolone to form the key Ir(V)-nitrenoid species, regioselective migratory insertion (C–N formation), and the final protodemetalation to give the amidation product and regenerate the active species. The results show that AgNTf$_2$ plays an important role in the formation of active species $[Cp*Ir(OAc)]^+$. As for the regioselectivity, in the key Ir(V)-nitrenoid species, both the weaker Ir–C(internal) bond and the shorter interatomic distance of N···C(internal) make the migratory insertion into Ir–C (internal) bond easier than Ir–C (terminal), leading to branch-selective allylic C–H amidation. By comparison of Cp*Ir(III)- and Cp*Co(III)-catalyzed processes, it is obvious that the higher catalytic activity of Ir complex is mainly attributed to the relative stability of alkene-coordinating π-complex and the stronger metal···H interaction assisting hydrogen transfer in comparison with Co system. The analyses of geometric parameters, frontier molecular orbital, bond indexes, and distortion-interaction offered insights into such catalytic systems. The result presented here could add better understanding to the mechanism, regioselectivity, and catalytic activity of transition-metal-catalyzed allylic C–H amination and is expected to be helpful for further development of regioselective C–H amination reactions.

Conflicts of interest

There are no conflicts to declare.

Acknowledgements

References

1 (a) K. Shin, H. Kim and S. Chang, *Acc. Chem. Res.*, 2015, **48**, 1040–1052; (b) P. Ruiz-Castillo and S. L. Buchwald, *Chem. Rev.*, 2016, **116**, 12564–12649; (c) R. Ma and M. C. White, *J. Am. Chem. Soc.*, 2018, **140**, 3202–3205; (d) M. D. Karkas, *Chem. Soc. Rev.*, 2018, **47**, 5786–5865; (e) K. Muniz, *Acc. Chem. Res.*, 2018, **51**, 1507–1519; (f) Y. Zhao and W. Xia, *Chem. Soc. Rev.*, 2018, **47**, 2591–2608; (g) O. I. Afanasyev, E. Kuchuk, D. L. Usanov and D. Chusov, *Chem. Rev.*, 2019, **119**, 11857–11911.

2 (a) J. L. Roizen, M. E. Harvey and J. Du Bois, *Acc. Chem. Res.*, 2012, **45**, 911–922; (b) M.-L. Louillat and F. W. Patureau, *Chem. Soc. Rev.*, 2014, **43**, 901–910; (c) T. Xiong and Q. Zhang, *Chem. Soc. Rev.*, 2016, **45**, 3069–3087; (d) H. Kim and S. Chang, *Acc. Chem. Res.*, 2017, **50**, 482–486; (e) Y. Park, Y. Kim and S. Chang, *Chem. Rev.*, 2017, **117**, 9247–

9301; (f) X. Qi, Y. Li, R. Bai and Y. Lan, *Acc. Chem. Res.*, 2017, **50**, 2799–2808.

3 (a) J. F. Hartwig, *Acc. Chem. Res.*, 2008, **41**, 1534–1544; (b) J. F. Hartwig, *Nature*, 2008, **455**, 314–322.

4 (a) R. Breslow and S. H. Gellman, *J. Chem. Soc., Chem. Commun.*, 1982, 1400–1401; (b) R. Breslow and S. H. Gellman, *J. Am. Chem. Soc.*, 1983, **105**, 6728–6729.

5 (a) P. Dydio, H. M. Key, H. Hayashi, D. S. Clark and J. F. Hartwig, *J. Am. Chem. Soc.*, 2017, **139**, 1750–1753; (b) K. Shing, Y. Liu, B. Cao, X. Chang, T. You and C. Che, *Angew. Chem., Int. Ed.*, 2018, **57**, 11947–11951; (c) A. Nasrallah, V. Boquet, A. Hecker, P. Retailleau, B. Darses and P. Dauban, *Angew. Chem., Int. Ed.*, 2019, **58**, 8192–8196; (d) R. Singh and A. Mukherjee, *ACS Catal.*, 2019, **9**, 3604–3617; (e) R. J. Harris, J. Park, T. A. F. Nelson, N. Iqbal, D. C. Salgueiro, J. Bacsa, C. E. MacBeth, M. H. Baik and S. B. Blakey, *J. Am. Chem. Soc.*, 2020, **142**, 5842–5851; (f) J. Lee, S. Jin, D. Kim, S. H. Hong and S. Chang, *J. Am. Chem. Soc.*, 2021, **143**, 5191–5200.

6 (a) E. N. Bess, R. J. DeLuca, D. J. Tindall, M. S. Oderinde, J. L. Roizen, J. Du Bois and M. S. Sigman, *J. Am. Chem. Soc.*, 2014, **136**, 5783–5789; (b) T. M. Figg, S. Park, J. Park, S. Chang and D. G. Musaev, *Organometallics*, 2014, **33**, 4076–4085; (c) G. Manca, E. Gallo, D. Intrieri and C. Mealli, *ACS Catal.*, 2014, **4**, 823–832; (d) S. H. Park, J. Kwak, K. Shin, J. Ryu, Y. Park and S. Chang, *J. Am. Chem. Soc.*, 2014, **136**, 2492–2502; (e) X. Zhang, H. Xu and C. Zhao, *J. Org. Chem.*, 2014, **79**, 9799–9811; (f) K. Hou, D. A. Hrovat and X. Bao, *Chem. Commun.*, 2015, **51**, 15414–15417; (g) M. J. Ajitha, K.-W. Huang, J. Kwak, H. J. Kim, S. Chang and Y. Jung, *Dalton Trans.*, 2016, **45**, 7980–7985; (h) M. Anand, R. B. Sunoj and H. F. Schaefer III, *ACS Catal.*, 2016, **6**, 696–708; (i) C. Kong, N. Jana, C. Jones and T. G. Driver, *J. Am. Chem. Soc.*, 2016, **138**, 13271–13280; (j) J. Wang, C. Zhao, Y. Weng and H. Xu, *Catal. Sci. Technol.*, 2016, **6**, 5292–5303; (k) H. Xu, X. Zhang, Z. Ke and C. Zhao, *RSC Adv.*, 2016, **6**, 29045–29053; (l) Y. Zhou and X. Bao, *Org. Lett.*, 2016, **18**, 4506–4509; (m) D. Fujita, H. Sugimoto, Y. Shiota, Y. Morimoto, K. Yoshizawa and S. Itoh, *Chem. Commun.*, 2017, **53**, 4849–4852; (n) B. E. Haines, T. Kawakami, K. Kuwata, K. Murakami, K. Itami and D. G. Musaev, *Chem. Sci.*, 2017, **8**, 988–1001; (o) P. F. Kuijpers, M. J. Tiekink, W. B. Breukelaar, D. L. J. Broere, N. P. van Leest, J. I. van der Vlugt, J. N. H. Reek and B. de Bruin, *Chem.–Eur. J.*, 2017, **23**, 7945–7952; (p) Z. Li, D. J. Burnell and R. J. Boyd, *J. Phys. Chem. B*, 2017, **121**, 10859–10868; (q) J. Wang, K. Zheng, B. Lin and Y. Weng, *RSC Adv.*, 2017, **7**, 34783–34794; (r) X. Zhang, *J. Organomet. Chem.*, 2017, **832**, 1–8; (s) D. Gao and X. Bao, *Org. Chem. Front.*, 2018, **5**, 1471–1482; (t) A. Varela-Alvarez, B. E. Haines and D. G. Musaev, *J. Organomet. Chem.*, 2018, **867**, 183–192; (u) P. Li and Z. Cao, *Organometallics*, 2018, **38**, 343–350; (v) Y. Hwang, H. Jung, E. Lee, D. Kim and S. Chang, *J. Am. Chem. Soc.*, 2020, **142**, 8880–8889; (w) Y. Yu, G. Luo, J. Yang and Y. Luo, *Catal. Sci. Technol.*, 2019, **9**, 1879–1890; (x) Y. Yu, G. Luo, J. Yang and Y. Luo, *Catal. Sci. Technol.*, 2020,

10, 1914–1924; (y) Y. Yu, G. Luo, J. Yang and Y. Luo, *Chin. J. Chem.*, 2020, **38**, 1526–1532.

7 (a) W. Zhang, N.-X. Wang and Y. Xing, *Synlett*, 2015, **26**, 2088–2098; (b) X. Yang, G. Shan, L. Wang and Y. Rao, *Tetrahedron Lett.*, 2016, **57**, 819–836; (c) J. C. K. Chu and T. Rovis, *Angew. Chem., Int. Ed.*, 2018, **57**, 62–101; (d) T. G. Saint-Denis, R.-Y. Zhu, G. Chen, Q. F. Wu and J.-Q. Yu, *Science*, 2018, **359**, eaao4798; (e) T. Knecht, S. Mondal, J. H. Ye, M. Das and F. Glorius, *Angew. Chem., Int. Ed.*, 2019, **58**, 7117–7121; (f) J. S. Burman, R. J. Harris, C. M. B. Farr, J. Bacsa and S. B. Blakey, *ACS Catal.*, 2019, **9**, 5474–5479.

8 (a) F. Liron, J. Oble, M. M. Lorion and G. Poli, *Eur. J. Org. Chem.*, 2014, **2014**, 5863–5883; (b) C. C. Pattillo, J. I. Strambeanu, P. Calleja, N. A. Vermeulen, T. Mizuno and M. C. White, *J. Am. Chem. Soc.*, 2016, **138**, 1265–1272; (c) R. Ma and M. C. White, *J. Am. Chem. Soc.*, 2018, **140**, 3202–3205; (d) R. Wang, Y. Luan and M. Ye, *Chin. J. Chem.*, 2019, **37**, 720–743.

9 M. S. Chen and M. C. White, *J. Am. Chem. Soc.*, 2004, **126**, 1346–1347.

10 (a) A. Archambeau and T. Rovis, *Angew. Chem., Int. Ed.*, 2015, **54**, 13337–13340; (b) Y. Shibata, E. Kudo, H. Sugiyama, H. Uekusa and K. Tanaka, *Organometallics*, 2016, **35**, 1547–1552; (c) J. S. Burman and S. B. Blakey, *Angew. Chem., Int. Ed.*, 2017, **56**, 13666–13669; (d) T. A. F. Nelson and S. B. Blakey, *Angew. Chem., Int. Ed.*, 2018, **57**, 14911–14915.

11 H. Lei and T. Rovis, *J. Am. Chem. Soc.*, 2019, **141**, 2268–2273.

12 M. J. Frisch, G. W. Trucks, H. B. Schlegel, G. E. Scuseria, M. A. Robb, J. R. Cheeseman, G. Scalmani, V. Barone, G. A. Petersson, H. Nakatsuji, X. Li, M. Caricato, A. V. Marenich, J. Bloino, B. G. Janesko, R. Gomperts, B. Mennucci, H. P. Hratchian, J. V. Ortiz, A. F. Izmaylov, J. L. Sonnenberg, D. Williams-Young, F. Ding, F. Lipparini, F. Egidi, J. Goings, B. Peng, A. Petrone, T. Henderson, D. Ranasinghe, V. G. Zakrzewski, J. Gao, N. Rega, G. Zheng, W. Liang, M. Hada, M. Ehara, K. Toyota, R. Fukuda, J. Hasegawa, M. Ishida, T. Nakajima, Y. Honda, O. Kitao, H. Nakai, T. Vreven, K. Throssell, J. A. Montgomery Jr, J. E. Peralta, F. Ogliaro, M. J. Bearpark, J. J. Heyd, E. N. Brothers, K. N. Kudin, V. N. Staroverov, T. A. Keith, R. Kobayashi, J. Normand, K. Raghavachari, A. P. Rendell, J. C. Burant, S. S. Iyengar, J. Tomasi, M. Cossi, J. M. Millam, M. Klene, C. Adamo, R. Cammi, J. W. Ochterski, R. L. Martin, K. Morokuma, O. Farkas, J. B. Foresman and D. J. Fox, *Gaussian* 16, Revision A.03, Gaussian, Inc., Wallingford, CT, 2016.

13 (a) A. D. Becke, *J. Chem. Phys.*, 1993, **98**, 1372–1377; (b) C. Lee, W. Yang and R. G. Parr, *Phys. Rev. B: Condens. Matter Mater. Phys.*, 1988, **37**, 785–789; (c) A. D. Becke, *Phys. Rev. A: At., Mol., Opt. Phys.*, 1988, **38**, 3098–3100.

14 S. Grimme, J. Antony, S. Ehrlich and H. Krieg, *J. Chem. Phys.*, 2010, **132**, 154104.

15 (a) M. Kaupp, P. V. Schleyer, H. Stoll and H. Preuss, *J. Chem. Phys.*, 1991, **94**, 1360–1366; (b) A. Henglein, *J. Phys. Chem.*, 1993, **97**, 5457–5471; (c) U. Steinbrenner, A. Bergner, M. Dolg and H. Stoll, *Mol. Phys.*, 1994, **82**, 3–11.

16 F. Weigend and R. Ahlrichs, *Phys. Chem. Chem. Phys.*, 2005, **7**, 3297–3305.

17 A. V. Marenich, C. J. Cramer and D. G. Truhlar, *J. Phys. Chem. B*, 2009, **113**, 4538–4543.

18 J. N. Harvey, M. Aschi, H. Schwarz and W. Koch, *Theor. Chem. Acc.*, 1998, **99**, 95–99.

19 C. Y. Legault, *CYLview, 1.0b*, Université de Sherbrooke, 2009, http://www.cylview.org.

20 Although some studies have shown that the acetate isomerization step is often more energy demanding than the C–H cleavage, the energy barrier of acetate isomerization *via* **Ir-TS_{iso}** is lower than that of the following C–H activation step (*via* **Ir-TS_3**) in current study. See refs: (a) A. de Aguirre, S. Díez-González, F. Maseras, M. Martín and E. Sola, *Organometallics*, 2018, **37**, 2645–2651; (b) D. L. Davies, S. A. Macgregor and A. I. Poblador-Bahamonde, *Dalton Trans.*, 2010, **39**, 10520–10527.

21 (a) Y. Park, J. Heo, M.-H. Baik and S. Chang, *J. Am. Chem. Soc.*, 2016, **138**, 14020–14029; (b) S. Y. Hong, Y. Hwang, M. Lee and S. Chang, *Acc. Chem. Res.*, 2021, DOI: 10.1021/acs.accounts.1c00198.

22 (a) F. Bickelhaupt and K. Houk, *Angew. Chem., Int. Ed.*, 2017, **56**, 10070–10086; (b) I. Fernández and F. Bickelhaupt, *Chem. Soc. Rev.*, 2014, **43**, 4953–4967; (c) F. Liu, Y. Liang and K. Houk, *Acc. Chem. Res.*, 2017, **50**, 2297–2308.